Filament Activation in Response to Magnetic Flux Emergence and Cancellation in Filament Channels

Ting Li[1] · Jun Zhang[1] · Haisheng Ji[2]

Abstract We make a comparative analysis for two filaments that showed quite different activation in response to the flux emergence within the filament channels. The observations from the *Solar Dynamics Observatory* (*SDO*) and Global Oscillation Network Group (GONG) are carried out to analyze the two filaments on 2013 August 17-20 and September 29. The first event showed that the main body of the filament was separated into two parts when an active region (AR) emerged with a maximum magnetic flux of about 6.4×10^{21} Mx underlying the filament. The close neighborhood and common direction of the bright threads in the filament and the open AR fan loops suggest similar magnetic connectivity of these two flux systems. The equilibrium of the filament was not destroyed within 3 days after the start of the emergence of the AR. To our knowledge, similar observations have never been reported before. In the second event, the emerging flux occurred nearby a barb of the filament with a maximum magnetic flux of 4.2×10^{20} Mx, about one order of magnitude less than that of the first event. The emerging flux drove the convergence of two patches of parasitic polarity in the vicinity of the barb, and resulted in cancellation between the parasitic polarity and nearby network fields. About 20 hours after the onset of the emergence, the filament was entirely erupted. Our findings imply that the location of emerging flux within the filament channel is probably crucial to filament evolution. If the flux emergence appears nearby the barbs, flux cancellation of emerging flux with the filament magnetic fields is prone to occur, which probably causes the filament eruption. The comparison of the two events shows that the emergence of an entire AR may still not be enough to disrupt the stability of a filament system and the actual eruption does occur only after the flux cancellation sets in.

Keywords: Prominences, Formation and Evolution; Prominences, Dynamics; Magnetic fields, Photosphere; Coronal Mass Ejections, Initiation and Propagation

[1] Key Laboratory of Solar Activity, National Astronomical
Observatories, Chinese Academy of Sciences, Beijing 100012,
China; email: liting@nao.cas.cn
[2] Key Laboratory for Dark Matter and Space Science,
Purple Mountain Observatory, CAS, Nanjing 210008, China

1. Introduction

The relationship between filament activation and the evolution of its surrounding magnetic fields is of great importance for understanding the triggering mechanisms of the activation (Wang et al. 1996; Schmieder et al. 2008; Kusano et al. 2012). Since the associated magnetic changes usually occur earlier than the filament activation (Jiang et al. 2007; Sterling et al. 2007; Xu et al. 2008), the evolution of magnetic fields in the filament environment can serve as an early signature for the occurrence of filament eruptions and the associated coronal mass ejections (CMEs).

The slow−rise motion of the filament before the rapid acceleration is frequently triggered by magnetic flux emergence or cancellation (Forbes & Isenberg 1991; Chen et al. 2009; Shen et al. 2011; Bi et al. 2013). The slow magnetic reconnection in the process of flux emergence and cancellation gradually changes the equilibrium state of a filament and usually results in the slow ascent of the filament (Chen & Shibata 2000; Lin et al. 2001; Zhang & Wang 2001; Nagashima et al. 2007). The newly emerging flux with a favorable orientation for reconnection with the preexisting flux is more likely to lead to an eruption than the one with an unfavorable orientation (Feynman & Martin 1995; Galsgaard et al. 2007). Jing et al. (2004) found that 54 events (68%) of 80 filament eruptions were accompanied by new flux emergence adjacent to eruptive filaments that usually appeared within 15 hr before filament eruptions.

Regarding the magnetic field topology of filaments, several models have been proposed so far (Mackay et al. 2010). In the empirical 'wire model,' the magnetic field lines of a filament are highly sheared along the magnetic polarity inversion line (PIL) and do not contain dips (Martin & Echols 1994; Lin et al. 2008). The magnetic fields supporting the barbs (plasma condensations) are vertical, connecting the filament body to parasitic (minority) polarity elements in the photosphere (Martin & Echols 1994; Lin et al. 2005). The parasitic polarity is defined as the polarity opposite to the dominant polarity of the network fields on the same side of the filament. In sheared arcade model (Antiochos et al. 1994; DeVore & Antiochos 2000) and flux rope model (van Ballegooijen & Martens 1989; Amari et al. 1999), the dense filament plasma lies in the dips of the magnetic fields. Aulanier et al. (1998, 1999) have developed 3D magnetic models of filaments and showed that the filaments can be represented by helical flux ropes overlying the PIL. The plasma of barbs is confined by the magnetic dips and the endpoints of barbs in the photosphere are located at secondary PIL separating the parasitic polarity from the surrounding dominant flux (Dudík et al. 2008).

In this work, we make a comparative analysis for two events focusing on the relationship between filament activation and flux emergence with the observations from the *Solar Dynamics Observatory* (*SDO*; Pesnell et al. 2012) and Global Oscillation Network Group (GONG). The first event showed that the main body of the filament was separated into two parts when an active region (AR) emerged within the filament channel. To our knowledge, the observations of filament separation due to an emerging AR underlying a filament have never been reported before. In the second event, the emerging flux happened to appear

in the vicinity of a barb, and subsequently resulted in a filament eruption. This rarely reported event gives us a good opportunity to study the interaction of the emerging flux with the magnetic structures of a barb and the physical process of how the evolution of a barb destabilizes the main body of the corresponding filament.

2. Observations and Data Analysis

The Atmospheric Imaging Assembly (AIA; Lemen et al. 2012) onboard the *SDO* takes full-disk images in 10 (E)UV channels at $1.5''$ resolution and high cadence of 12 s. The observations of 304 Å, 171 Å and 193 Å are used in this study. The channel of 304 Å (He II) corresponds to a temperature of about 0.05 MK, 171 Å (Fe IX) at 0.6 MK, and the 193 Å channel (Fe XII) is at 1.5 MK (with a hot contribution of Fe XXIV at 20 MK, Ca XVII at 6.0 MK and cooler O V at 0.2 MK; O'Dwyer et al. 2010; Del Zanna 2013). In order to investigate the interaction of emerging flux with the ambient magnetic structures, we also use the full-disk line-of-sight magnetic field data from the Helioseismic and Magnetic Imager (HMI; Scherrer et al. 2012) onboard *SDO*, with a cadence of ~ 3 min and a sampling of $0.5''$ pixel^{-1}. NSO$-$GONG Hα data are used to investigate the chromospheric configuration of the filament. GONG collects Hα data at seven sites with a spatial resolution of $1.0''$ pixel^{-1} and a cadence of around 1 min (Harvey et al. 2011).

3. Results

3.1. The First Event (2013 August 17$-$20)

The first event analyzed here occurred on 2013 August 17$-$20. A large filament lies across the entire south hemisphere (Figure 1(d); see Animation 0817-304). It has a length of about 992 Mm, and is located between AR 11818 and AR 11820. Starting from 04:00 UT on August 17, new magnetic flux emerged in the filament channel. The two patches with opposite polarities gradually grew up and evolved into AR 11824 (Figures 1(a)-(c)). Seen from AIA 304 Å observations, the emergence of magnetic flux is associated with EUV intensity enhancement and no barbs are observed nearby the region of flux emergence (Figures 1(e) and (f)). From 10:00 UT on August 17, the main body of the filament was gradually divided into two parts (Figures 1(d)$-$(f)). Due to the interaction between the AR and the filament, the south end of the north filament is located in the vicinity of the emerged positive polarity fields and the north end of the south filament is located nearby the emerged negative polarity fields (Figure 1(c)).

In Hα images (Figures 2(a)-(b)), the north part of the filament is much fainter than that in EUV wavelength (Figures 1(d)-(f)). Nearby the emerging AR, the filament in Hα is fragmented and the connectivity could not be clearly observed. The difference in Hα and EUV images can be ascribed to more abundant Lyman continuum absorption in EUV than in Hα and the effect of the coronal emissivity
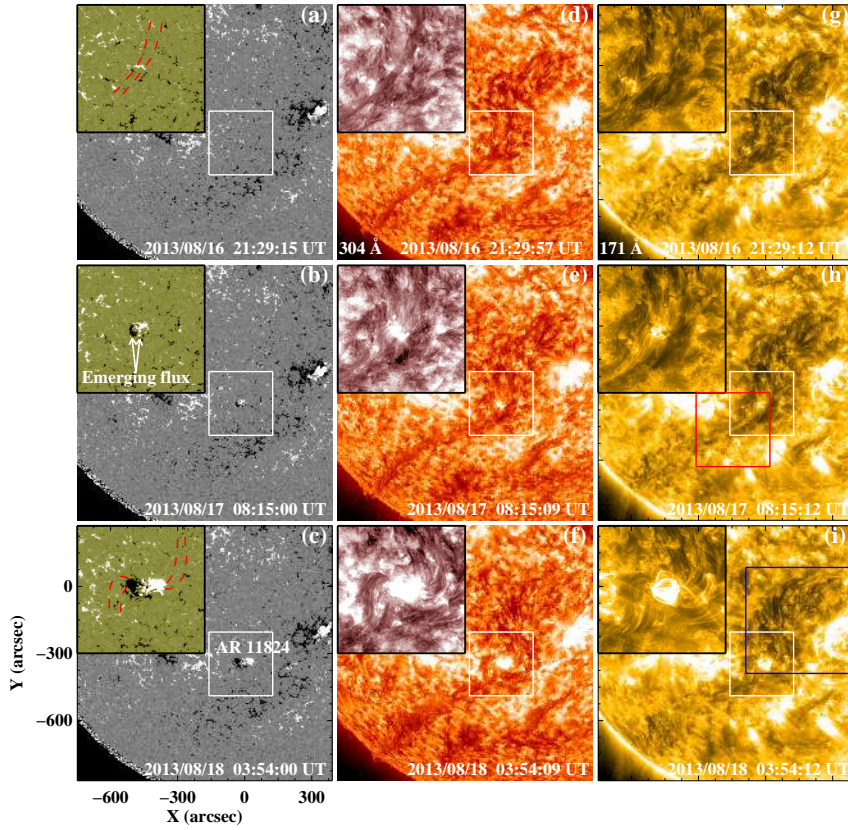
Figure 1. *SDO*/HMI line-of-sight magnetograms showing the emerging magnetic flux within the filament channel (panels (a)−(c)), AIA 304 Å and 171 Å images showing the evolution of the filament (panels (d)−(i); see Animation 0817-304) during 2013 August 16−18. The upper-left corner in each panel shows the enlarged image in the white square. The red dashed lines in panels (a) and (c) denote the contours of the filament. The red square in panel (h) denotes the field of view (FOV) of Figures 3(a)−(f). The blue square in panel (i) denotes the FOV of Figures 3(g)−(l).

blocking due to the prominence void (Wang et al. 1998; Heinzel et al. 2001, 2008; Schmieder et al. 2003; Anzer & Heinzel 2005; Li & Zhang 2013a). Only the low and denser parts of the filament may be visible in Hα on the disk (Heinzel et al. 2001). The appearances of the filament at 171 Å and 193 Å are shown in Figures 1(g)−(i) and 2(d)−(f). The 171 Å band can contain bright threads along the filament channel due to the Fe IX line being in emission in the high-temperature transition region (Parenti et al. 2012). The EUV filament channel is more extended than the filament because of the local relative absence of plasma with coronal densities and temperatures (i.e., a 'void'; Heinzel et al. 2008).
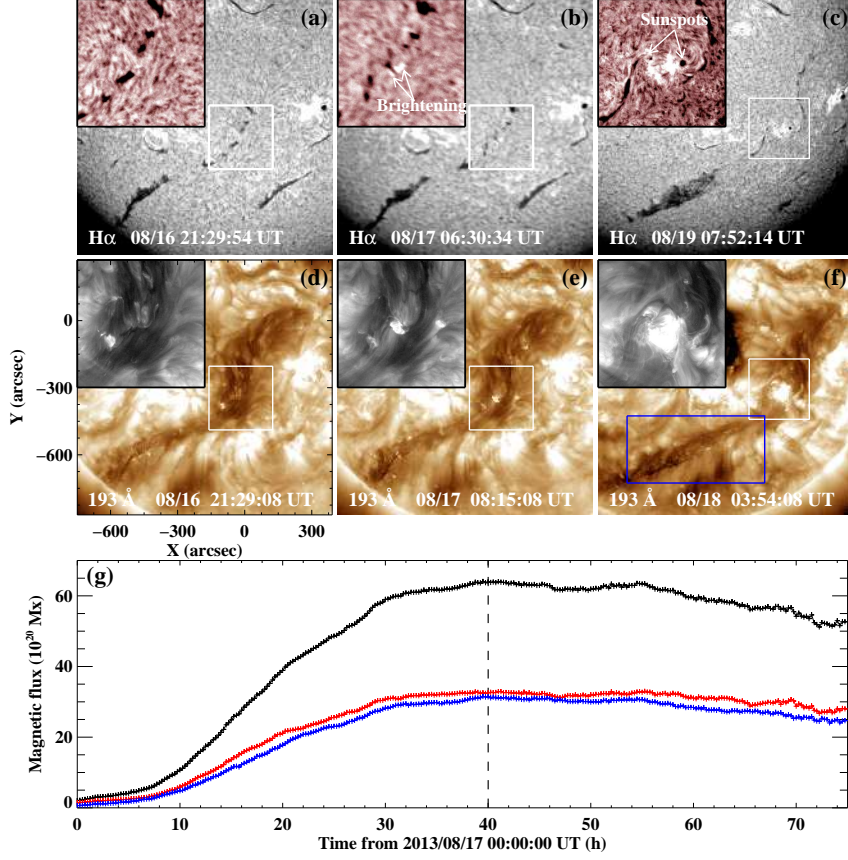
Figure 2. Appearance of the first event in GONG Hα (panels (a)−(c)) and AIA 193 Å (panels (d)−(f)) and temporal variations of the emerging magnetic flux in HMI magnetograms (panel (g)). The upper-left corner in each panel shows the enlarged image in the white square. The blue rectangular in panel (f) denotes the FOV of EUV and Hα images in Figure 5. The black profile in panel (g) denotes the evolution of total magnetic flux and the red and blue profiles denote the unsigned positive and negative magnetic flux. Dashed line in panel (g) denotes the time when the total unsigned magnetic flux reached its maximum.

The magnetic flux gradually emerged underlying the filament and the intensity enhancement in Hα was simultaneously observed (Figures 2(b)-(c)). Despite the emergence of the AR, the filament was stable and did not erupt during August 18-19 (Figures 2(c) and (f)). The Hα filament is clearly visible in close vicinity of the southeast and northwest parts of AR 11824. The leading and following sunspots are formed at the emerging region (Figure 2(c)). The leading sunspot has positive polarity fields and the following one has negative polarity fields (Figure 1(c)).
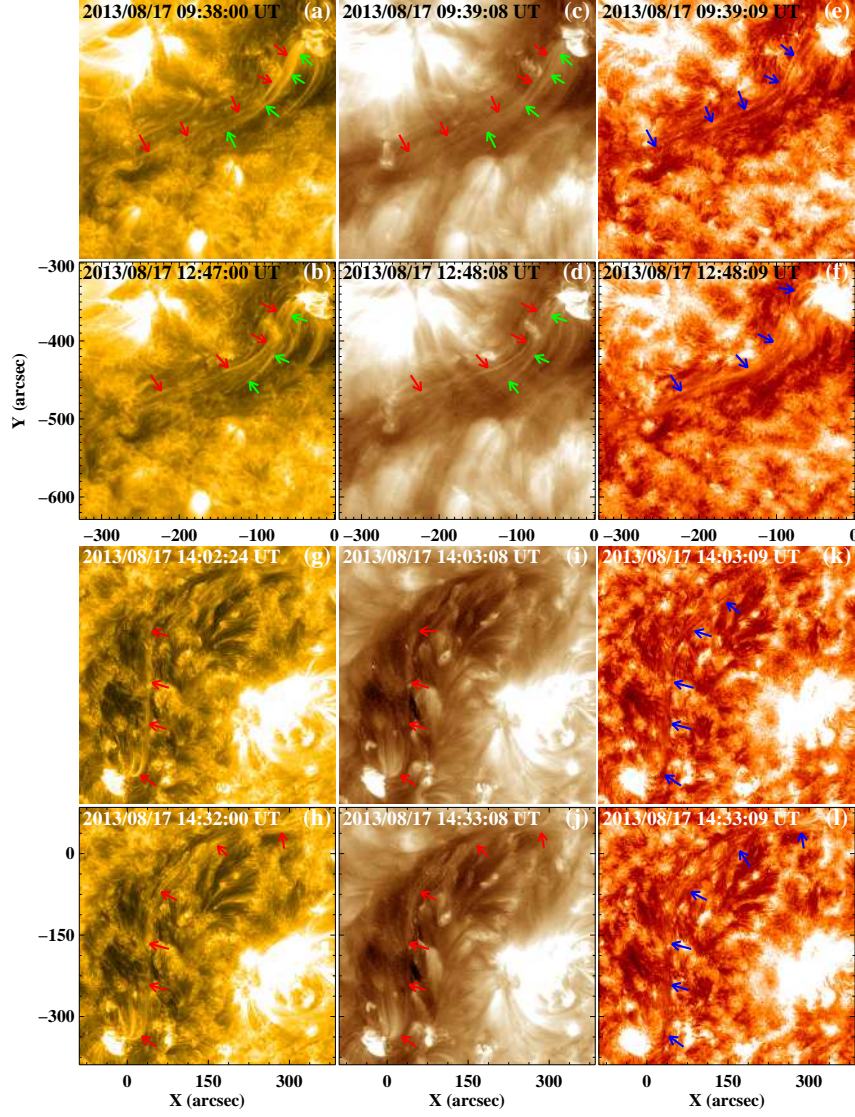
Figure 3. *SDO*/AIA 171, 193 and 304 Å images showing the fine-scale structures of the southern (panels (a)−(f)) and northern (panels (g)−(l)) filaments. The FOV of panels (a)−(f) is the red square in Figure 1(h), and the FOV of panels (g)−(l) corresponds to the blue square in Figure 1(i). The arrows point to the bright threads in the filament.
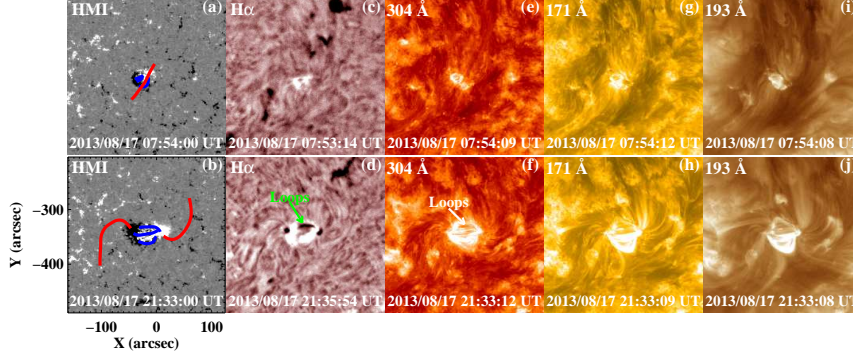
Figure 4. Appearance of the filament and the closed loops of the AR in HMI magnetograms, GONG Hα, AIA 304, 171 and 193 Å images. Red solid curves in panels (a) and (b) denote the axes of the filament as seen in 304 Å images and blue solid curves represent the closed loops of the AR. The FOV of these images is denoted by the white square in Figures 1 and 2.

The temporal variations of the emerging magnetic flux in HMI magnetograms were measured and are displayed in Figure 2(g). We derotated all the magnetograms differentially to a reference time (2013 August 17 00:00 UT). The area within which we calculated the magnetic flux is changed according to the expansion of the emerging AR to ensure that the area has an appropriate size (Yang et al. 2012). Due to the expansion of the emerging flux during 3 days, a pre-selected fixed box could not exactly contain the AR. If the box is larger, other magnetic structures are also included. If the box is smaller, the AR at the late stage is beyond the area of the box. After selection, the pixels with unsigned magnetic fields weaker than 10.2 Mx cm^{-2} (noise level determined by Liu et al. 2012) are eliminated. Moreover, the actual magnetic flux is approximately $\Phi/\cos(\alpha_0) \times \cos(\alpha)$ due to the projection effects, where α_0 is the heliocentric angle at the reference time, α is the heliocentric angle at the observation time and Φ is the observed magnetic flux. Here, we used the equation to eliminate projection effects due to differential rotation during construction of magnetic flux plots.

The temporal profiles of unsigned positive and negative magnetic flux show consistent trend. The emergence lasted for about 36 hr and the total magnetic flux increased to 6.4×10^{21} Mx at 16:00 UT on August 18. This is a smaller AR by comparing its unsigned magnetic flux with typical unsigned fluxes of ARs in Warren et al. (2012). The maximum values of positive and negative magnetic flux are nearly equal, about 3.2×10^{21} Mx. The average flux emergence rate is approximately 2.3×10^{16} Mx s^{-1}. Afterwards, the positive and negative magnetic flux gradually decreased and the morphologies of the north and south filaments remained steady. At 03:00 UT on Aug 20, the total unsigned magnetic flux decreased by 26% within 35 hr.

At 09:09 UT on Aug 17, about 5 hr after the start of the flux emergence, bright fine-scale threads could be clearly observed at the southeast of the AR, with its end anchoring in the negative polarity fields (Figures 3(a)-(f); Figure
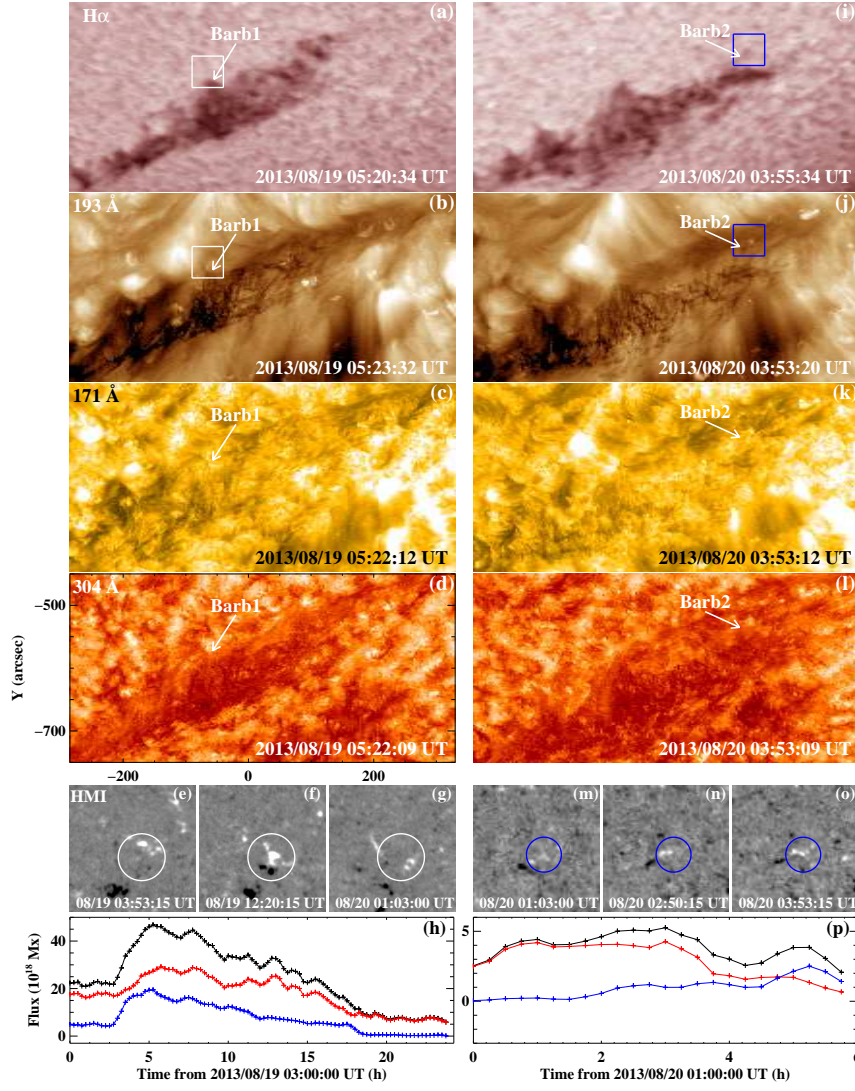
Figure 5. GONG Hα images, AIA 193, 171, 304 Å images, HMI magnetograms and temporal variations of the magnetic flux showing two barbs of the southern filament and the evolution of magnetic fields. The FOV of GONG Hα and EUV images is represented by the blue rectangular in panel (f) of Figure 2. The white square in panels (a)-(b) denotes the FOV of panels (e)−(g) and the blue square in panels (i)-(j) denotes the FOV of panels (m)−(o). White circles outline the flux emergence and cancellation nearby the Barb1, and blue circles outline the flux emergence nearby the Barb2. The meanings of the profiles in panels (h) and (p) are the same as those in Figure 2(g).

1(b)). These bright threads extended from the AR to the southeast within the filament channel. The 171 Å band best shows the bright threads that are fainter at 193 and 304 Å. Similar bright threads could be observed in the northern part of the filament channel (Figures 3(g)-(j)). The ends of the threads are located at the positive polarity fields (see Figure 1(c)). The 304 Å observations also show dark fine-scale threads of the filament connecting the AR with the north end of the filament (Figures 3(k)-(l)). Accompanying the interaction of the AR with the filament, the previous long filament was divided into two parts, with the ends located nearby the two opposite polarity fields of the AR. The long threads in the filament channel usually could be observed in the passbands of 304 Å, 171 Å and 193 Å. Thus the observed bright structures may contain both the threads within the filament itself and the skewed fan loops with one footpoint rooting in one polarity of the AR.

Moreover, the bright and dark closed loops appeared in the emerging AR (Figure 4). The emerging AR showed a clockwise rotation and the filament was cut into two parts, which formed two 'S' shaped structures. The closed loops were located between the two 'S' shaped structures (new north and south filaments). With the evolution of the AR, the south leg of the north filament and the north leg of the south filament were becoming more curved around the AR.

From about 05:30 UT on August 19, other small-scale magnetic flux (Figures 5(e)-(f)) emerged nearby the Barb1 of the south filament. Meanwhile, the EUV intensity enhancement at 304, 171 and 193 Å was observed near the Barb1 and the brightenings in Hα could not be clearly observed. The temporal variation of the emerging magnetic flux is shown in panel (h). At 08:00 UT, the unsigned magnetic flux increased to its maximum of about 4.7×10^{19} Mx. Then the emerged flux gradually canceled with nearby magnetic fields and the unsigned magnetic flux decreased to 5.9×10^{18} Mx at 01:00 UT on August 20 (panels (g)-(h)). Another magnetic flux emerged nearby the Barb2 from 01:00 UT on August 20 (panels (m)-(p)). The emerging magnetic fields are weak and have an unsigned magnetic flux of 5.0×10^{18} Mx. These small-scale magnetic fields seemed to disturb the stability of the southern filament. At about 04:00 UT on August 20, the south filament started to rise up slowly and erupted partially. The filament eruption caused a CME with an average velocity of 490 km s^{-1} in the FOV of Large Angle and Spectrometric Coronagraph (LASCO; Brueckner et al. 1995) C2. The filament eruption was not accompanied by any X-ray flare.

3.2. The Second Event (2013 September 29)

In the second event on 2013 September 29, the lateral barb of the filament could be clearly identified at AIA 304, 171 and 193 Å and Hα observations (Figure 6; see Animation 0929-304). In Hα observations, the filament is composed of two strands intertwined with each other (Figure 6(d), similar to the observations of Liu et al. (2008)). From about 00:00 UT on September 29, the magnetic flux emerged in the vicinity of the barb within the filament channel (Figures 6(a)-(c)). The emergence of magnetic flux is associated with EUV intensity enhancement at AIA 171 and 193 Å (Figures 6(k) and (n)), which indicates coronal emission rather than absorption by the filament material (Anzer & Heinzel 2005). The

brightening could not be clearly observed in Hα and 304 Å (Figures 6(e) and (h)). After the emergence, a destabilization of the filament occurred near the barb and resulted in the eruption of the filament (Hα and EUV images in right column of Figure 6). The entire eruptive filament could be observed in EUV passbands, however, only the north part of the filament appears in Hα during the eruption (panel (f)).

At the onset of flux emergence, multiple pairs of small magnetic patches with opposite polarities dispersedly appeared and the positive and negative magnetic fields were interwoven together (Figures 7(a)-(c)). Then the small patches with the same polarity converged and merged into a large and concentrated magnetic structure (Figure 7(d)). The emerging magnetic flux could be identified as a dipolar region after 08:00 UT (Figure 7(e)). In the vicinity of the barb's end, small patches of parasitic polarity were observed (denoted by arrows 'P1' and 'P2' in panel (a)). The flux emergence drove the converging motion of magnetic structure 'P2' toward 'P1,' which merged together into a large magnetic structure 'P3' (panel (c)). Afterward, the positive magnetic structure 'P3' constantly canceled with nearby negative network fields (such as magnetic structures 'N1' and 'N2' in panels (c) and (g)). In 193 and 304 Å images, the material of the barb appeared as multiple thread-like structures (Figure 8). Meanwhile, bi-directional mass flows could also be observed along the axis of the barb. At 20:24 UT, the barb was elongated and the filament started to rise up slowly (Figures 8(g) and (l)). The flux cancellation of the emerging magnetic flux ('EN' and 'EP') with nearby magnetic structures constantly occurred (red circles in Figure 8(b)). After 21:20 UT, the filament was accelerated and erupted rapidly.

In order to investigate the kinematic evolution of the filament in detail, we obtained the stack plots at 193 and 304 Å (Figures 9(a)-(b)) along slice 'A−B' (Figure 6(g)). Both the filament main body and its barb could be clearly observed in the stack plots. At about 18:40 UT, a surge seemed to appear in the vicinity of the barb (Figure 9(b)). This surge may be related to the later filament eruption. By tracing a single thread of the filament main body in the stack plot at 304 Å, velocity−time and acceleration−time profiles of the filament main body were obtained (black and green curves in Figure 9(c)). Since about 20:30 UT, the filament started to rise up with a small velocity less than 3 km s^{-1}. From 21:00 UT, the velocity showed an obvious increase. At 21:20 UT, the velocity reached about 17 km s^{-1} with the acceleration of 15 m s^{-2}. Due to the uncertainty of thread location (about 3 pixel), the uncertainty of the velocity was estimated about 1.0 km s^{-1}. The velocity of the barb thread is shown by the red curve in panel (c). In the early phase, the velocities of the two threads in the barb and the filament main body are nearly the same and their difference is within the error of the velocity. From about 20:45 UT, the velocity of the barb thread is lower than that of the thread in the filament main body. This indicates that the filament main body drags the barb along with it. Until 21:30 UT, the barb seemed to be divided into two parts, with the lower part remaining stable and the top part suddenly rising up (the time interval between two dashed lines in Figures 9(a)-(b); Figures 8(i) and (n)). The rising barb threads were brightened during the eruption process (Figure 9(b)), and these bright threads were probably heated by magnetic reconnection occurring underlying the filament. The velocity of
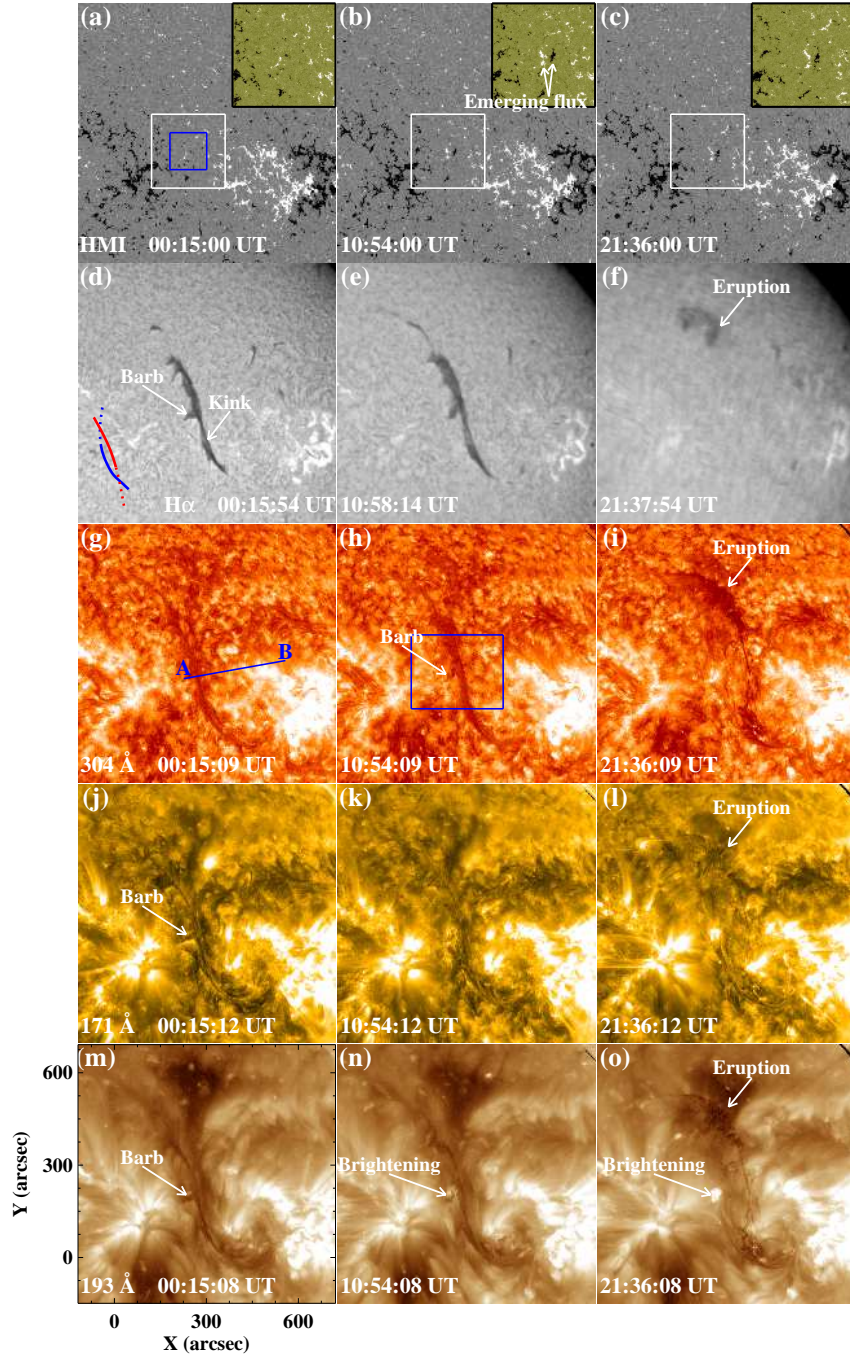
Figure 6. *SDO*/HMI magnetograms, GONG Hα, AIA 304, 171 and 193 Å images (see Animation 0929-304) showing the emergence of magnetic flux and the evolution of the filament on 2013 September 29. The upper-right corner in panels (a)-(c) shows the enlarged image in the white square. The blue square in panel (a) denotes the FOV of Figure 7. The blue rectangular in panel (h) denotes the FOV of Figure 8. The straight line 'A−B' in panel (g) is used to obtain the stack plots in Figures 9(a)-(b).
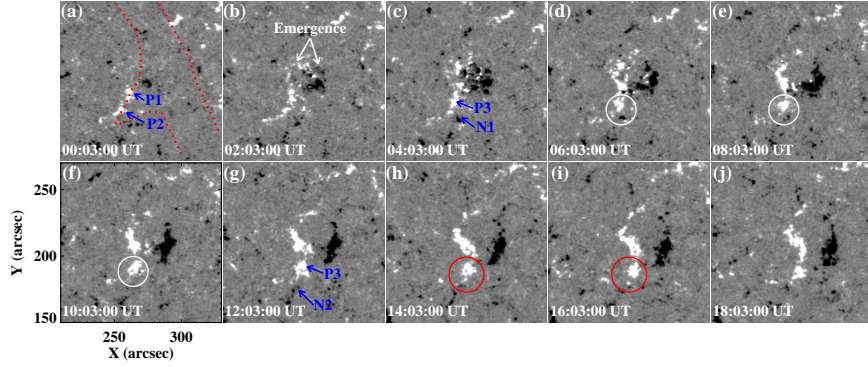
Figure 7. Evolution of the magnetic structures in the vicinity of the barb in the second event. The FOV of HMI magnetograms is represented by the blue square in Figure 6(a). The red dotted curves in panel (a) denote the filament contours. Magnetic structures 'P1' and 'P2' denote the parasitic magnetic polarities nearby the barb. Magnetic structures 'P1' and 'P2' merge together into a larger one 'P3'. Positive magnetic structure 'P3' cancels with negative magnetic structures 'N1' (outlined by white circles) and 'N2' (outlined by red circles).

the threads in the filament main body and the velocity of the top barb are approximately equal to each other after 21:30 UT. Then the filament main body erupted rapidly and its velocity increased to 170 km s^{-1} (the projected velocity; the corresponding vertical velocity is about 340 km s^{-1}) and the acceleration reached about 260 m s^{-2} at 21:48 UT. About 30 min later (22:12 UT), LASCO C2 observed a CME with an angular width of 160 degree and an average speed of 680 km s^{-1}. The filament eruption was also associated with a C1.2 flare that started at 21:43 UT.

As seen from Figure 9(d), the magnetic flux of new emerging bipole is calculated. The emerging flux in the filament channel of the second event is about one order of magnitude less than that of the first event. At about 10:00 UT, the total magnetic flux increased to a maximum of 4.2×10^{20} Mx. The values of positive and negative magnetic flux are approximately balanced (red and blue curves). The average flux emergence rate is nearly 5.2×10^{15} Mx s^{-1}, about one fourth of the first event. Until about 17:00 UT, the magnetic flux maintained at a relatively steady value. Then the emerged magnetic flux showed an obvious decrease due to the constant cancellation with nearby opposite magnetic fields. By comparing the kinematic evolution of the filament with the temporal variations of emerging magnetic flux, we noticed that the eruption of the filament occurred in the decaying phase of the emerging magnetic flux, with a time delay of more than 20 hr from the start of the emergence.

4. Summary and Discussion

We make a comparative analysis for two filaments that showed quite different activation in response to the flux emergence within the filament channels. In the first event, an AR emerged below the filament with a maximum magnetic
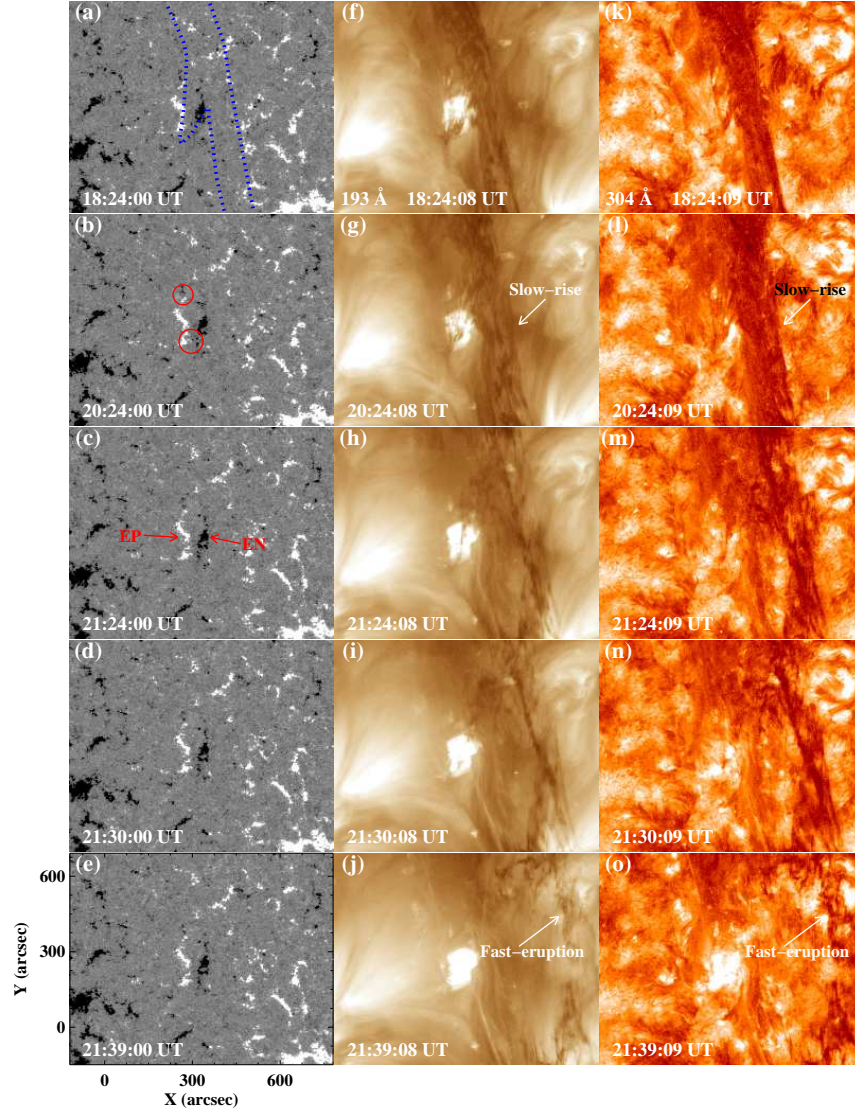
Figure 8. Evolution of the emerging flux and the barb prior and during the eruption of the filament. The FOV of HMI magnetograms, *SDO*/AIA 193 and 304 Å images is represented by the blue rectangular in Figure 6(h). The blue dotted curves in panel (a) denote the filament contours. Magnetic structures 'EP' and 'EN' denote the emerging positive and negative magnetic fields. Red circles outline the cancellation of the emerging magnetic flux ('EN' and 'EP') with nearby magnetic structures.
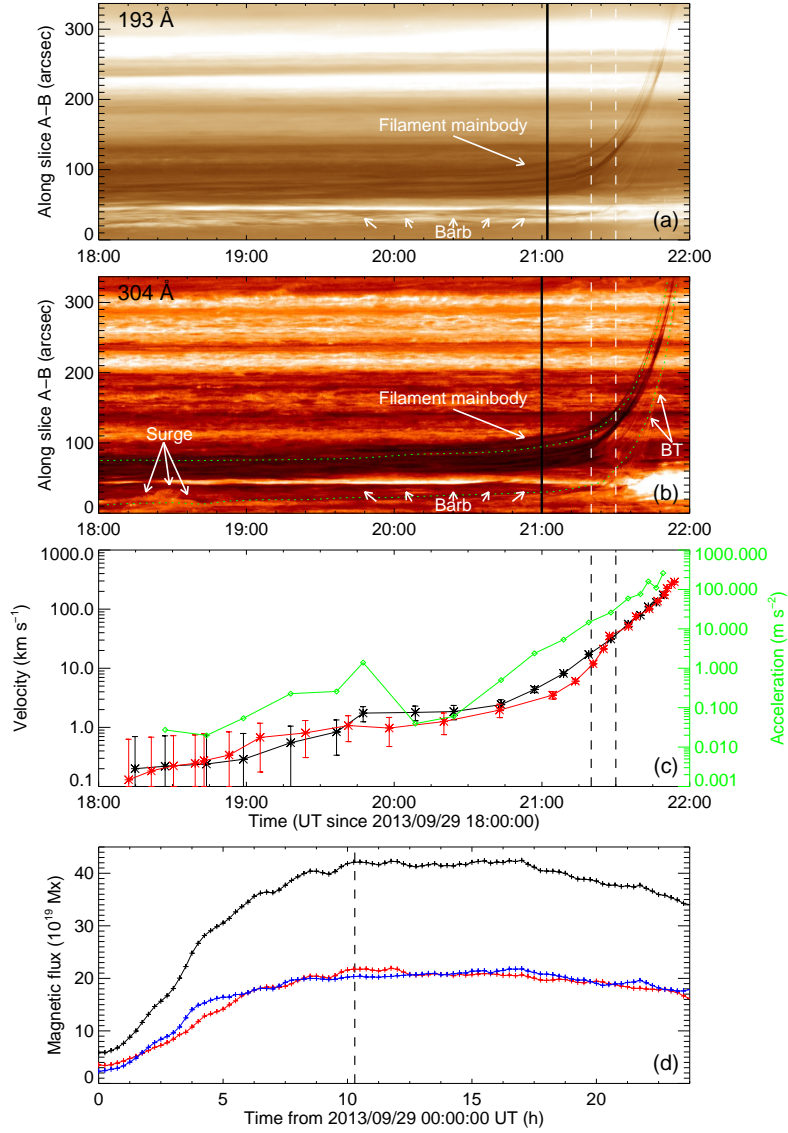
Figure 9. Panel (a)-(b): stack plots along slice 'A−B' (blue line in Figure 6(g)) showing the evolution of the filament at AIA 193 and 304 Å. Two green dotted curves in panel (b) denote two threads of the filament main body and the barb that are used for velocity measurements in panel (c). 'BT' denotes the bright threads during the eruption process. Panel (c): velocity-time (black curve), acceleration-time profiles (green curve) of a single thread of the filament main body based on panel (b), and the velocity of the barb threads (red curve). Dashed lines in panels (a)-(c) denote the transition time between the slow-rise and fast-rise phases. Panel (d): temporal variations of the unsigned positive (red curve), negative (blue curve), and total (black curve) emerging magnetic flux. Dashed line in panel (d) denotes the time when the total unsigned magnetic flux reached its maximum.

flux of about 6.4×10^{21} Mx. The emerging flux resulted in the separation of the filament into two parts, with the south end of the north part located nearby the emerged positive polarity fields and the north end of the south part in the emerged negative ones. Due to the interaction of the emerging flux with the filament, bright fine-scale threads within the filament channel extending from the AR towards two opposite directions are clearly observed (Figure 3). This is the firstly reported example that the filament is separated into two parts due to an emerging AR within the filament channel. In Hα images, the filament is fragmented and the connectivity could not be clearly observed. Comparison of the AIA 304 Å images with Hα images (Figures 1 and 2) shows that the chromospheric configuration of the filament could only be observed if the optical depth in Hα is large enough. A similar example was presented in Li & Zhang (2013a), in which the spine of the filament can only be detected in 304 Å images.

For the first event, the filament did not erupt within 3 days, instead, it was separated into two parts (north and south filaments). The close neighborhood and common direction of the bright threads in the filament and the open AR fan loops suggest similar magnetic connectivity of these two flux systems. These threads in both parts of the filament may imply the configuration of the magnetic field lines (Li & Zhang 2013b; Joshi et al. 2014). On the 3rd and 4th day after the emergence of the AR , the AR started to decay. Near that time, the emergence and cancellation of other small magnetic polarities occurred nearby the barbs of the southern filament. These small-scale magnetic fields seemed to disturb the stability of the south filament, which resulted in the partial eruption of the filament. The statistics showed that the shorter distance between the new active regions and quiescent filaments, the less time between active region appearance and filament disappearance (Bruzek 1952; Balasubramaniam et al. 2011). Thus the time interval of 4 days is too long and it is not reasonable to correlate the AR emergence within the filament channel with the later eruption. A case of filament eruption on the 4th day after a new flux emergence away from the filament channel was analyzed by Feynman & Martin (1995). The active region continued to emerge on the day of the eruption and they attributed the eruption to the flux emergence. However, in our first event, the AR emergence ceased about 2 days before the eruption. We suggest that the eruption of the south filament is caused by the emergence and cancellation of the small-scale magnetic flux (Figure 5) nearby the barbs about 20 hr before its eruption.

In the second event, the emerging flux occurred nearby a barb of the filament with a maximum magnetic flux of 4.2×10^{20} Mx, about one order of magnitude less than that of the first event. The flux emergence probably caused the global destabilization of the filament and resulted in the final eruption of the entire filament about 20 hr after the start of flux emergence. By investigating the HMI magnetograms, it was found that the emerging flux drove the convergence of two patches of parasitic polarity in the vicinity of the barb. The cancellation between the parasitic polarity and nearby network fields was also observed. The evolution (flux convergence and cancellation) of parasitic polarity nearby the barb probably affected the stability of the filament. The velocity of the thread in the filament main body is larger than that of the barb thread. This indicates that the global destabilization of the filament is triggered and the filament main body

drags the barb along with it. However, the former case (barb pushing the main body) would be a strong evidence for flux near the barb leading to destabilization of the filament. The main body of the filament in the second event underwent a transition from slow-rise phase to fast-rise phase. The velocity of the filament increased to 170 km s^{-1} and the acceleration reached about 260 m s^{-2} about 20 min after the start of the fast-rise phase.

According to the models of Aulanier et al. (1998, 1999) and Dudík et al. (2008), the plasma of barbs are supported by magnetic dips that are formed due to the presence of parasitic polarities in the filament channel. The change of the parasitic patches nearby the barbs is responsible for the evolution of barbs. In our study, the observed flux convergence and cancellation of parasitic polarity disturbed the magnetic fields passing through the barb, and the tether-cutting reconnection (Moore et al. 2001) between the field lines supporting the barb material (magnetic dips nearby the barb) and nearby network fields might be triggered. Then the stability of the filament was catastrophically destroyed and the filament was erupted rapidly.

The relation of flux emergence and the filament eruption has been analyzed in previous studies (Sun et al. 2012; Mandrini et al. 2014). Joshi et al. (2011) found the coincidence of the X-ray precursor phase with the flux emergence at the flaring location, and suggested that the flux emergence and pre-flare activities played a crucial role in destabilizing the filament. In our work, the AR in the first event emerged within the filament channel and the filament did not erupt within 3 days. No barbs of the filament are observed nearby the emerging AR. Afterwards, the emergence and cancellation of small-scale magnetic flux occurred nearby the barbs and the south filament erupted. For the second event, the emerging magnetic flux nearby the barb followed by flux cancellation resulted in the filament eruption about 20 hr later despite the fact that the emerging flux was one order of magnitude less than that of the AR in the first event. Our findings imply that the location of emerging flux within the filament channel is probably crucial to filament evolution. If the flux emergence appears nearby the barbs, flux cancellation of emerging flux with the filament magnetic fields is prone to occur. The flux cancellation results in the tethers to cut and reconnection to take place beneath the filament (Vemareddy et al. 2012; Kuridze et al. 2013; Huang et al. 2014; Jing et al. 2014). Thus flux emergence/cancelation and tether-cutting reconnection around the barbs of the filament cause the destabilization of the filament and the onset of its eruption. If the flux emergence within the filament channel is far away from the barbs, the occurrence of flux cancellation between emerging flux and the filament magnetic fields is not easy, and the equilibrium of filament is not destroyed. The comparison of the two events shows that the emergence of an entire AR may still not be enough to disrupt the stability of a filament system and the actual eruption does occur only after the flux cancellation sets in. Zuccarello et al. (2014) observed flux cancellation toward the compact polarity inversion line during the 8-10 hr preceding the eruption. Sterling et al. (2010) also suggested that the main filament ejection was triggered by flux cancelation between the positive flux elements and the surrounding negative field. In our work, the filament eruptions studied are associated with flux emergence, but occur only after completion of the emergence and/or after the

onset of the magnetic cancellation following the emergence. Although we do not perform modelling of the magnetic field of the filaments and their barbs, our observations of the emergence followed by cancellation in relation to the timing of filament eruptions add to the debate on the mechanism behind destabilization of solar structures. More samples need to be thoroughly analyzed to obtain a statistic about the relationships between filament evolution and flux emergence and cancellation in the filament environment.

References

Amari, T., Luciani, J. F., Mikic, Z., Linker, J.: 1999, Three-dimensional Solutions of Magneto-hydrodynamic Equationsfor Prominence Magnetic Support: Twisted Magnetic Flux Rope. *Astrophys. J. Lett.* **518**, L57.

Antiochos, S. K., Dahlburg, R. B., Klimchuk, J. A.: 1994, The magnetic field of solar prominences. *Astrophys. J. Lett.* **420**, L41

Anzer, U., Heinzel, P.: 2005, On the Nature of Dark Extreme Ultraviolet Structures Seen by SOHO/EIT and TRACE. *Astrophys. J.* **622**, 714

Aulanier, G., Demoulin, P.: 1998, 3-D magnetic configurations supporting prominences. I. The natural presence of lateral feet. *Astron. Astrophys.* **329**, 1125

Aulanier, G., Démoulin, P., Mein, N., et al.: 1999, 3-D magnetic configurations supporting prominences. III. Evolution of fine structures observed in a filament channel. *Astron. Astrophys.* **342**, 867

Balasubramaniam, K. S., Pevtsov, A. A., Cliver, E. W., Martin, S. F., Panasenco, O.: 2011, The Disappearing Solar Filament of 2003 June 11: A Three-body Problem. *Astrophys. J.* **743**, 202

Bi, Y., Jiang, Y., Yang, J., et al.: 2013, Analysis of the Simultaneous Rotation and Non-radial Propagation of an Eruptive Filament. *Astrophys. J.* **773**, 162

Brueckner, G. E., Howard, R. A., Koomen, M. J., et al.: 1995, The Large Angle Spectroscopic Coronagraph (LASCO). *Solar Phys.* **162**, 357

Bruzek, A.: 1952, On a type of flare associated with ascendant dark filaments. The Observatory, **72**, 154

Chen, H., Jiang, Y., Ma, S.: 2009, An EUV Jet and Halpha Filament Eruption Associated with Flux Cancellation in a Decaying Active Region. *Solar Phys.* **255**, 79

Chen, P. F., Shibata, K.: 2000, An Emerging Flux Trigger Mechanism for Coronal Mass Ejections. *Astrophys. J.* **545**, 524

Del Zanna, G.: 2013, The multi-thermal emission in solar active regions. *Astron. Astrophys.* **558**, A73

DeVore, C. R., Antiochos, S. K.: 2000, Dynamical Formation and Stability of Helical Prominence Magnetic Fields. *Astrophys. J.* **539**, 954

Dudík, J., Aulanier, G., Schmieder, B., Bommier, V., Roudier, T.: 2008, Topological Departures from Translational Invariance along a Filament Observed by THEMIS. *Solar Phys.* **248**, 29

Feynman, J., Martin, S. F.: 1995, The initiation of coronal mass ejections by newly emerging magnetic flux. *J. Geophys. Res.* **100**, 3355

Forbes, T. G., Isenberg, P. A.: 1991, A catastrophe mechanism for coronal mass ejections. *Astrophys. J.* **373**, 294

Galsgaard, K., Archontis, V., Moreno-Insertis, F., Hood, A. W.: 2007, The Effect of the Relative Orientation between the Coronal Field and New Emerging Flux. I. Global Properties. *Astrophys. J.* **666**, 516

Harvey, J. W., Bolding, J., Clark, R., et al.: 2011, Bulletin of the American Astronomical Society, **1745**

Heinzel, P., Schmieder, B., Fárník, F., et al.: 2008, Hinode, TRACE, SOHO, and Ground-based Observations of a Quiescent Prominence. *Astrophys. J.* **686**, 1383

Heinzel, P., Schmieder, B., Tziotziou, K.: 2001, Why Are Solar Filaments More Extended in Extreme-Ultraviolet Lines than in Halpha? *Astrophys. J. Lett.* **561**, L223

Huang, Z., Madjarska, M. S., Koleva, K., et al.: 2014, Halpha spectroscopy and multiwavelength imaging of a solar flare caused by filament eruption. *Astron. Astrophys.* **566**, 148

Jiang, Y.-C., Shen, Y.-D., Wang, J.-X.: 2007, Eruption of an Active-Region Filament Driven by an Emerging Bipole. *Chin. J. Astron. Astrophys.* **7**, 129

Jing, J., Liu, C., Lee, J., et al.: 2014, Evolution of a Magnetic Flux Rope and its Overlying Arcade Based on Nonlinear Force-free Field Extrapolations. *Astrophys. J. Lett.* **784**, L13

Jing, J., Yurchyshyn, V. B., Yang, G., Xu, Y., Wang, H.: 2004, On the Relation between Filament Eruptions, Flares, and Coronal Mass Ejections. *Astrophys. J.* **614**, 1054

Joshi, B., Veronig, A. M., Lee, J., et al.: 2011, Pre-flare Activity and Magnetic Reconnection during the Evolutionary Stages of Energy Release in a Solar Eruptive Flare. *Astrophys. J.* **743**, 195

Joshi, N. C., Srivastava, A. K., Filippov, B., et al.: 2014, Confined Partial Filament Eruption and its Reformation within a Stable Magnetic Flux Rope. *Astrophys. J.* **787**, 11

Kuridze, D., Mathioudakis, M., Kowalski, A. F., et al.: 2013, Failed filament eruption inside a coronal mass ejection in active region 11121. *Astron. Astrophys.* **552**, A55

Kusano, K., Bamba, Y., Yamamoto, T. T., et al.: 2012, Magnetic Field Structures Triggering Solar Flares and Coronal Mass Ejections. *Astrophys. J.* **760**, 31

Lemen, J. R., Title, A. M., Akin, D. J., et al. 2012, The Atmospheric Imaging Assembly (AIA) on the Solar Dynamics Observatory (SDO). *Solar Phys.* **275**, 17

Li, L., Zhang, J.: 2013a, The Evolution of Barbs of a Polar Crown Filament Observed by SDO. *Solar Phys.* **282**, 147

Li, T., Zhang, J.: 2013b, Fine-scale Structures of Flux Ropes Tracked by Erupting Material. *Astrophys. J. Lett.* **770**, L25

Lin, J., Forbes, T. G., Isenberg, P. A.: 2001, Prominence eruptions and coronal mass ejections triggered by newly emerging flux. *J. Geophys. Res.* **106**, 25053

Lin, Y., Martin, S. F., Engvold, O.: 2008, Filament Substructures and their Interrelation. Subsurface and Atmospheric Influences on Solar Activity, **383**, 235

Lin, Y., Wiik, J. E., Engvold, O., Rouppe van der Voort, L., Frank, Z. A.: 2005, Solar Filaments and Photospheric Network. *Solar Phys.* **227**, 283

Liu, R., Gilbert, H. R., Alexander, D., Su, Y.: 2008, The Effect of Magnetic Reconnection and Writhing in a Partial Filament Eruption. *Astrophys. J.* **680**, 1508

Liu, Y., Hoeksema, J. T., Scherrer, P. H., et al.: 2012, Comparison of Line-of-Sight Magnetograms Taken by the Solar Dynamics Observatory/Helioseismic and Magnetic Imager and Solar and Heliospheric Observatory/Michelson Doppler Imager. *Solar Phys.* **279**, 295

Mackay, D. H., Karpen, J. T., Ballester, J. L., Schmieder, B., Aulanier, G.: 2010, Physics of Solar Prominences: II-Magnetic Structure and Dynamics. *Space Sci. Rev.* **151**, 333

Mandrini, C. H., Schmieder, B., Démoulin, P., Guo, Y., Cristiani, G. D.: 2014, Topological Analysis of Emerging Bipole Clusters Producing Violent Solar Events. *Solar Phys.* **289**, 2041

Martin, S. F., Echols, C. R.: 1994, An observational and conceptual model of the magnetic field of a filament. Solar Surface Magnetism, 339

Moore, R. L., Sterling, A. C., Hudson, H. S., Lemen, J. R.: 2001, Onset of the Magnetic Explosion in Solar Flares and Coronal Mass Ejections. *Astrophys. J.* **552**, 833

Nagashima, K., Isobe, H., Yokoyama, T., et al.: 2007, Triggering Mechanism for the Filament Eruption on 2005 September 13 in NOAA Active Region 10808. *Astrophys. J.* **668**, 533

O'Dwyer, B., Del Zanna, G., Mason, H. E., Weber, M. A., Tripathi, D.: 2010, SDO/AIA response to coronal hole, quiet Sun, active region, and flare plasma. *Astron. Astrophys.* **521**, A21

Parenti, S., Schmieder, B., Heinzel, P., Golub, L.: 2012, On the Nature of Prominence Emission Observed by SDO/AIA. *Astrophys. J.* **754**, 66

Pesnell, W. D., Thompson, B. J., Chamberlin, P. C.: 2012, The Solar Dynamics Observatory (SDO). *Solar Phys.* **275**, 3

Scherrer, P. H., Schou, J., Bush, R. I., et al.: 2012, The Helioseismic and Magnetic Imager (HMI) Investigation for the Solar Dynamics Observatory (SDO). *Solar Phys.* **275**, 207

Schmieder, B., Bommier, V., Kitai, R., et al.: 2008, Magnetic Causes of the Eruption of a Quiescent Filament. *Solar Phys.* **247**, 321

Schmieder, B., Tziotziou, K., Heinzel, P.: 2003, Spectroscopic diagnostics of an Halpha and EUV filament observed with THEMIS and SOHO. *Astron. Astrophys.* **401**, 361

Shen, Y.-D., Liu, Y., Liu, R.: 2011, A time series of filament eruptions observed by three eyes from space: from failed to successful eruptions. Research in Astronomy and Astrophysics, **11**, 594

Sterling, A. C., Chifor, C., Mason, H. E., Moore, R. L., Young, P. R.: 2010, Evidence for magnetic flux cancelation leading to an ejective solar eruption observed by Hinode, TRACE, STEREO, and SoHO/MDI. *Astron. Astrophys.* **521**, A49

Sterling, A. C., Harra, L. K., Moore, R. L.: 2007, New Evidence for the Role of Emerging Flux in a Solar Filament's Slow Rise Preceding Its CME-producing Fast Eruption. *Astrophys. J.* **669**, 1359

Sun, X., Hoeksema, J. T., Liu, Y., et al.: 2012, Evolution of Magnetic Field and Energy in a Major Eruptive Active Region Based on SDO/HMI Observation. *Astrophys. J.* **748**, 77

van Ballegooijen, A. A., Martens, P. C. H.: 1989, Formation and eruption of solar prominences. *Astrophys. J.* **343**, 971

Vemareddy, P., Maurya, R. A., Ambastha, A.: 2012, Filament Eruption in NOAA 11093 Leading to a Two-Ribbon M1.0 Class Flare and CME. *Solar Phys.* **277**, 337

Wang, H., Chae, J., Gurman, J. B., Kucera, T. A.: 1998, Comparison of Prominences in Halpha and He II 304 Å. *Solar Phys.* **183**, 91

Wang, J., Shi, Z., Martin, S. F.: 1996, Filament disturbance and associated magnetic changes in the filament environment. *Astron. Astrophys.* **316**, 201

Warren, H. P., Winebarger, A. R., Brooks, D. H.: 2012, A Systematic Survey of High-temperature Emission in Solar Active Regions. *Astrophys. J.* **759**, 141

Xu, X. Y., Fang, C., Chen, P. F.: 2008, A Statistical Study on the Filament Eruption Caused by New Emerging Flux. Chinese Astron. Astrophys. **32**, 56

Yang, S., Zhang, J., Li, T., Liu, Y.: 2012, Self-cancellation of Ephemeral Regions in the Quiet Sun. *Astrophys. J. Lett.* **752**, L24

Zhang, J., Wang, J.: 2001, Filament Eruptions and Halo Coronal Mass Ejections. *Astrophys. J.* **554**, 474

Zuccarello, F. P., Seaton, D. B., Mierla, M., et al.: 2014, Observational Evidence of Torus Instability as Trigger Mechanism for Coronal Mass Ejections: The 2011 August 4 Filament Eruption. *Astrophys. J.* **785**, 88